Matter and
Radiation at Extremes

RESEARCH ARTICLE

pubs.aip.org/aip/mre

Temperature and structure measurements of heavy-ion-heated diamond using *in situ* X-ray diagnostics

Cite as: Matter Radiat. Extremes 9, 047802 (2024); doi: 10.1063/5.0203005
Submitted: 8 February 2024 • Accepted: 19 May 2024 •
Published Online: 12 June 2024

J. Lütgert,[1,a)] P. Hesselbach,[2,3] M. Schörner,[1] V. Bagnoud,[2] R. Belikov,[4] P. Drechsel,[2] B. Heuser,[1,5] O. S. Humphries,[5,6] P. Katrik,[2] B. Lindqvist,[1] C. Qu,[1] R. Redmer,[1] D. Riley,[7] G. Schaumann,[8] S. Schumacher,[1] A. Tauschwitz,[2] D. Varentsov,[2] K. Weyrich,[2] X. Yu,[2,9] B. Zielbauer,[2] Zs. Major,[2,10] P. Neumayer,[2] and D. Kraus[1,5,b)]

AFFILIATIONS

[1] Institut für Physik, Universität Rostock, Albert-Einstein-Str. 23, 18059 Rostock, Germany
[2] GSI Helmholtzzentrum für Schwerionenforschung, Planckstr. 1, 64291 Darmstadt, Germany
[3] Institut für Angewandte Physik, Goethe-Universität Frankfurt am Main, Max-von-Laue-Str. 1, 60438 Frankfurt am Main, Germany
[4] Institut für Geowissenschaften, Goethe-Universität Frankfurt am Main, Altenhöferallee 1, 60438 Frankfurt am Main, Germany
[5] Helmholtz-Zentrum Dresden-Rossendorf, Bautzner Landstr. 400, 01328 Dresden, Germany
[6] European XFEL GmbH, Holzkoppel 4, 22869 Schenefeld, Germany
[7] Centre for Plasma Physics, School of Mathematics and Physics, Queen's University Belfast, University Road, Belfast BT7 1NN, United Kingdom
[8] Institut für Kernphysik, Technische Universität Darmstadt, Schlossgartenstr. 9, 64289 Darmstadt, Germany
[9] State Key Laboratory of Nuclear Physics and Technology, Institute of Heavy Ion Physics, Peking University, Beijing 100871, China
[10] Helmholtz Institut Jena, Fröbelstieg 3, 07743 Jena, Germany

[a)] **Author to whom correspondence should be addressed:** julian.luetgert@uni-rostock.de
[b)] **Electronic mail:** dominik.kraus@uni-rostock.de

ABSTRACT

We present *in situ* measurements of spectrally resolved X-ray scattering and X-ray diffraction from monocrystalline diamond samples heated with an intense pulse of heavy ions. In this way, we determine the samples' heating dynamics and their microscopic and macroscopic structural integrity over a timespan of several microseconds. Connecting the ratio of elastic to inelastic scattering with state-of-the-art density functional theory molecular dynamics simulations allows the inference of average temperatures around 1300 K, in agreement with predictions from stopping power calculations. The simultaneous diffraction measurements show no hints of any volumetric graphitization of the material, but do indicate the onset of fracture in the diamond sample. Our experiments pave the way for future studies at the Facility for Antiproton and Ion Research, where a substantially increased intensity of the heavy ion beam will be available.

I. INTRODUCTION

X-ray diagnostics have proven to be a powerful tool to probe high-energy-density matter, in order to access its structure, temperature, ionization state, or density, which are crucial for understanding a variety of plasma processes.[1] Techniques such as *in situ* spectrally resolved X-ray scattering (also called X-ray Thomson scattering, XRTS, in the community) and X-ray diffraction (XRD) have been widely applied as sensitive probes of bulk characteristics.[2–7] These diagnostics are complementary to optical methods, which only provide information on the sample surface and fail completely once the matter has become opaque to visible light.

The latter is the case in the warm dense matter (WDM) regime, where densities are comparable to ambient conditions and temperatures are of the order of typical binding energies. The study of WDM is a rapidly expanding field in modern physics, investigating matter in the transient regime between the solid and plasma states. Not only can WDM be found in many astrophysical objects,[8–10] it also promises new methods for material synthesis.[11,12] Both computational and experimental improvements over the last decades now allow the simulation and measurement of the behavior of these exotic states of matter that have previously been inaccessible.

The generation of WDM states in the laboratory is most commonly based on shocks—utilizing different drivers, ranging from gas guns[13] and Z-pinches[14] to lasers.[15,16] These setups inherently lead to small samples with short lifetimes on the nanosecond scale. As a novel and complementary approach, the use of heavy ions for generating WDM has recently been proposed, in connection with the Facility for Antiproton and Ion Research (FAIR), currently under construction in Darmstadt, Germany.[17]

With the expected ion numbers, samples of millimeter size can be heated to temperatures of more than ~10 eV and studied over a significantly longer timescale of hundreds of nanoseconds or even several microseconds. Owing to these longer timescales, the heated region is also expected to reach local thermal equilibrium,[17] which has to be carefully verified when analyzing shock-driven WDM states.

For the diagnostics of heavy-ion-heated material, the implementation of X-ray diagnostics for temperature and structural observations is desirable, but this imposes new challenges. In this paper, we report on the first results using laser-generated X rays to perform simultaneous *in situ* XRTS and XRD measurements on samples heated by heavy ions.

We chose monocrystalline diamond as the system to be investigated in this scenario. In an evacuated oven, a volumetric transition of diamond to graphite can be observed over a timespan exceeding minutes at temperatures above ~1900 K, with the rate of graphitization rapidly increasing with temperature.[18,19] Alternatively, such a change in structure can be induced locally, by depositing over ~1.2 eV on a single atom.[20] Theoretical calculations predict partial graphitization to occur within several hundreds of femtoseconds for such experiments.[21] However, the energy threshold for the transition and its speed are subjects of active research.[20–23] In our study, we explore the hitherto poorly investigated intermediate-time regime—and also different mechanisms, since the ions interact not only with electrons but also directly with the diamond lattice.

A better understanding of the durability of a heated diamond lattice at ambient pressures on microsecond timescales also has several direct implications. First, the bombardment of diamond with fast ions is a typical scenario at GSI, FAIR, and other accelerator facilities, where this material is used within the sensors of particle detectors owing to its mechanical and electronic properties.[24] Information on the material's stability under these conditions is therefore of practical importance. Second, such knowledge would be beneficial in the case of nanodiamonds from laser-driven shock experiments, where their formation can be probed *in situ* using XRD[10,11] but their recovery has yet to be achieved.[25]

The experiment was performed at the GSI Helmholtzzentrum für Schwerionenforschung (Darmstadt, Germany), using the heavy ions of the SIS18 heavy ion synchrotron and the nanosecond pulse of the PHELIX high-energy laser facility for generating the X rays for the diagnostics. Using this existing infrastructure allows for testing and improving methods and diagnostics for future operation of FAIR, in what is also termed the FAIR Phase-0 research program.

We infer the temperature of our sample from the ratio of elastic to inelastic scattering in the XRTS diagnostic by comparison with density functional theory molecular dynamics (DFT-MD) simulations (see Sec. III). A simultaneous XRD measurement finds no evidence for graphitization, but might indicate a macroscopic fracture of the sample (Sec. IV). Our results show that with the currently available ion numbers, the sample is heated to temperatures around 1300 K, which is too cold to study WDM. However, with FAIR coming online in the future, more than tenfold higher temperatures are expected to be reached,[26] for which the method presented here can also be applied.

II. EXPERIMENTAL SETUP

The experimental study was carried out in the framework of experiment S489 at GSI in the HHT (high-energy, high-temperature) experiment area. The full experimental setup is described by Hesselbach *et al.*,[27] and the PHELIX capabilities can be found in Major *et al.*[28] Here, we focus on the XRD and XRTS findings of the experiment.

Our full target assembly consisted of three main components enclosed in a milled aluminum housing: a monocrystalline diamond disk of 3 mm diameter and 60 μm thickness, a gold pinhole of 0.5 mm diameter, located a distance of 1.5 mm from the diamond, and finally a 10 μm-thick titanium foil, an additional 1.5 mm behind the pinhole, for creating the probing X rays (see Fig. 1).

To heat the diamond, we used a beam of $^{208}\text{Pb}^{67+}$ ions with 450 MeV/u, provided by GSI's SIS18 accelerator. To increase the energy deposition within the sample, the ions were decelerated using a 15 mm-thick slab of PMMA upstream of the target. Simulations with SRIM[29] predict a beam energy of ~288 MeV/u after this degrader slab. Within a pulse of 250–300 ns full-width half-maximum (FWHM), $\sim 3.4 \times 10^9$ ions were focused to a spot of two-dimensional Gaussian shape with FWHM of $0.6 \times 0.9\ \text{mm}^2$.

For probing our target, the PHELIX laser delivered 100–130 J at 527 nm wavelength onto the titanium backlighter foil to generate 4.75 keV He_α emission. We focused the optical beam with a lens of

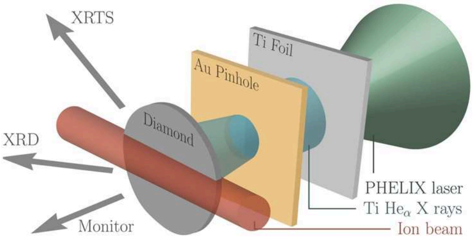

FIG. 1. Schematic of experimental setup. He_α emission was generated from a titanium backlighter foil by irradiating it with the PHELIX beam. A gold pinhole aperture was installed to collimate the X rays, which then illuminated the monocrystalline diamond sample. Three X-ray diagnostic instruments were fielded to investigate the material during and after the heating by the lead ion beam: an X-ray Thomson spectrometer (XRTS), an imaging plate recording the diffraction pattern (XRD), and a monitor spectrometer recording the spectrum of the X-ray source.

1.8 m focal length, achieving a spot size of ~30–40 μm FWHM. The pulse duration amounted to 2 ns, resulting in an intensity of (3–8) × 10^{15} W/cm^2. The X rays were recorded by three diagnostics:

(a) A monitor spectrometer, located at an angle of 0°, recording the backlighter source. This spectrometer consisted of a planar highly oriented pyrolytic graphite (HOPG) crystal with a mosaicity of 0.25° and 100 μm thickness.

(b) The X-ray Thomson spectrometer at a scattering angle of 135° in Von Hámos geometry,[30] using a cylindrically bent HOPG with a radius of 50 mm, a thickness of 100 μm, and a mosaicity of 0.5°. Both spectrally resolved diagnostics used Greateyes CCD detectors to record the signal.

(c) An imaging plate (IP; GE Healthcare BAS IP SR 2040 E), positioned at a distance of (422 ± 4) mm from the diamond at an angle of (70.7 ± 1.5)°, to record the diffraction signal around the (111) Laue spot. To ensure that the peak was covered by the ~ 15 × 15 cm^2 area of the IP, we rotated the diamond accordingly, before mounting it on the target, since the cylinder surfaces were oriented in the (100) direction.

As we found that irradiating the target with ions resulted in a notable background, we shielded the direct line of sight of the digital detectors to the target with metal blocks and installed several layers of aluminum and Mylar foils in front of the spectrometers' entrance windows, the detector chips, and also the IP. To further reduce parasitic signal from charged particles, we deployed magnets with B-field strengths of 0.55 T (XRTS) and 0.4 T (XRD) in front of the X-ray diagnostics.

III. X-RAY THOMSON SCATTERING

During the scattering of a photon on an electron, the momentum transfer $k = |\mathbf{k}_s - \mathbf{k}_0|$ can be approximated by $k \approx (2\omega_0/c)\sin(\theta/2)$ if the induced change in frequency is small, i.e., $\omega = \omega_0 - \omega_s \ll \omega_0$. Here, $\mathbf{k}_0$ and ω_0 are the wave vector and angular frequency of the incoming light, $\mathbf{k}_s$ and ω_s are those of the scattered light, c is the speed of light, and θ is the scattering angle.

The intensity of the scattered light is proportional to the total static electron structure factor $S_{ee}^{\mathrm{tot}}(k)$, which is commonly decomposed into three contributions:[31,32]

$$S_{ee}^{\mathrm{tot}}(k) = S_{ee}^{\mathrm{ion}}(k) + S_{ee}^{\mathrm{bf}}(k) + S_{ee}^{\mathrm{free}}(k), \tag{1}$$

where the three terms describe elastic scattering (S_{ee}^{ion}), inelastic scattering due to bound-free transitions (S_{ee}^{bf}) and inelastic scattering on free—or nearly free—electrons (S_{ee}^{free}), respectively. For the temperatures reached in our experiment, all electrons remain bound to the atom, and so the last term in this equation can be omitted. Neglecting the screening by free electrons for the same reason, and assuming the L shell ionization energy to be small compared with the Compton energy, Eq. (1) can be rewritten as[15,31,33,34]

$$S_{ee}^{\mathrm{tot}}(k) = \underbrace{|f(k)|^2 S_{ii}(k)}_{\text{elastic}} + \underbrace{\sum_{n=1}^{Z_{\mathrm{wb}}}\left[1 - f_n^2(k)\right]}_{\text{inelastic}}. \tag{2}$$

Here, the ionic form factor f and the ion–ion structure factor S_{ii} have been introduced. The sum in Eq. (2) runs over all electrons for which the binding energy is smaller than the energy transfer in the scattering process $\hbar\omega$, namely, the four electrons in the carbon L shell for our setup. f_n denotes the contribution of a single electron to f, which is sometimes approximated as being identical for all electrons.[34] In this work, however, we use analytical functions that assume hydrogen-like atoms, giving different contributions depending on the electrons' principal and azimuthal quantum numbers.[35] The ratio of elastic to inelastic scattering $x_{\mathrm{el}}/x_{\mathrm{inel}}$, a quantity directly accessible in experiments, is hence connected to the static ion–ion structure factor by[15]

$$S_{ii}(k) = \frac{1}{|f(k)|^2}\left(\sum_{n=1}^{Z_{\mathrm{wb}}}\left[1 - f_n^2(k)\right]\right)\frac{x_{\mathrm{el}}}{x_{\mathrm{inel}}}. \tag{3}$$

At ambient temperatures, the nearly perfect lattice structure of a monocrystalline sample results in clear Laue spots that contain nearly all coherently scattered light. Hence, an XRTS spectrometer, covering a scattering vector range for which no such peak is expected, will mainly record an inelastic signal. When the target is heated, the described behavior changes. With increased movement of atoms in the lattice, more photons are scattered coherently to scattering angles where no Laue spot is expected, and hence the elastic signal on the detector rises.

Therefore, we can leverage XRTS measurements as a temperature diagnostic by fitting the ratio of elastic to inelastic signal, calculating S_{ii} using analytical approximations for the f_n.[35] This value can then be compared with results of state-of-the-art DFT-MD simulations for the sample material at a given temperature (see Fig. 2). Our method provides valuable benefits over the well-established technique of optical pyrometry, since the X-ray based diagnostic is still sensitive at lower temperatures, where the former approach is severely limited on the fast timescale of dynamic experiments. In contrast to pyrometry—which can only infer the temperature at the sample surface—XRTS provides insight into the bulk and is therefore well suited for the volumetric heating achieved by ion beams.

Applying the method to our setup, DFT-MD calculations predict the ratio of elastic to inelastic scattering from ambient diamond to amount to ~1.7% for the probed scattering vector lengths around $k = 4.45$ Å^{-1}. Heating the sample to a temperature of 3000 K increases this value by a factor of ~10 (shown in the inset of Fig. 2). This sensitivity enables us to investigate temperatures where volumetric graphitization by heating has been observed.[18] Furthermore, the simulations predict a linear scaling of the ratio with temperature, simplifying the analysis. For more details concerning our DFT-MD calculations, we refer to Appendix A.

Despite various efforts to shield and deflect particles produced by the ion beam (see Sec. II and Ref. 27), the recorded spectra are dominated by parasitic signal. We attribute this to particles generated by the ion beam interacting with our target, the PMMA degrader, and the entrance window of the chamber. To clean the data, we first subtracted a background by averaging over regions on the detector far from the focal line of the spectrometer crystal. We then removed hard hits and strong, connected signal, guided by a neural network. More details on this step can be found in Appendix C.

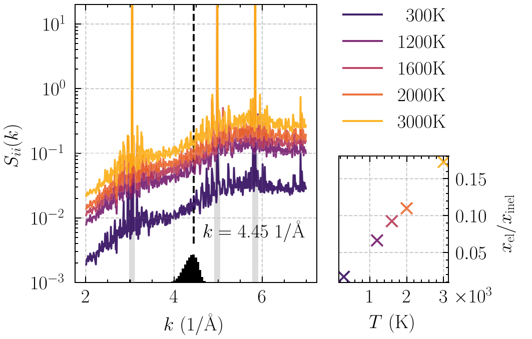

FIG. 2. Ion–ion structure factor $S_{\mathrm{ii}}(k)$ for a diamond lattice at different temperatures calculated by DFT-MD. The gray lines indicate Bragg reflections. Our XRD diagnostic measured diffraction from the first peak. The black histogram shows the range of scattering vector lengths k covered in our XRTS setup. The inset on the right visualizes the predicted ratio $x_{\mathrm{el}}/x_{\mathrm{inel}}$ of elastic to inelastic scattering, calculated with Eq. (3) for this k distribution. The simulation suggests a linear increase in elastic scattering with a ratio ∼10 times higher for 3000 K compared with ambient conditions.

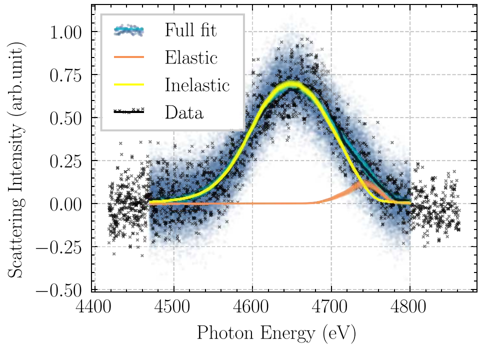

FIG. 3. Posterior predictions modeling the spectrally resolved XRTS signal (black) as the sum of an elastic (orange) and inelastic (yellow) contribution. The latter two curves were obtained by simulating the experiment using our ray tracing code with input from DFT-MD in the case of the incoherent curve. The full model (blue) additionally assumed a Gaussian noise with constant unknown magnitude. To guide the eye, smoothed curves of the noisy data and full predictions are plotted as solid lines.

The scattering data were fitted as the sum of an inelastic and an elastic contribution. To simulate the former, we calculated the energy shift of inelastically scattered photons using linear response time-dependent DFT (LR-TDDFT), by computing the dielectric function and connecting it to S_{ee}^{bf} and S_{ee}^{free} (where the contribution of the latter is small for the reasons mentioned above) via the fluctuation–dissipation theorem.[36] To also obtain the instrument-free elastic scattering spectrum, we simulated the emission of the laser-driven titanium plasma using the commercially available PrismSPECT software,[37] benchmarked to the monitor spectrometer (see the supplementary material).

To account for the point-spread functions of our diagnostics, we relied on a ray tracing simulation of the setup. The software was written in Python using the package `jax`,[38] enabling us to consider a high number of rays in parallel while keeping the computation time manageable. The simulation of the mosaic crystals in our spectrometers was inspired by the `mmpxrt` code of Šmíd *et al.*[39] By simulating the full setup, we include the effects of broadening of the signal due to the finite X-ray spot size on the diamond, the dispersion and focusing of the mosaic crystal, and the backlighter spectrum. Supplementary descriptions of the ray tracing simulations are given in Appendix B.

We implemented a Bayesian fitting routine using `PyMC`[40] to obtain the ratio of elastic to inelastic scattering, assuming Gaussian noise with constant but unknown standard deviation. A comparison of the one-dimensional data and the posterior predictions of the fit is presented in Fig. 3 for a representative event.

By changing the delay between the SIS18 beam and the PHELIX pulse, we can investigate how the interaction with the heavy ions changes the scattering spectrum at—virtually—any time during or after the exposure to the ions. In the study presented, we recorded data up to a delay of 20 µs (see Fig. 4). The blue data points were obtained with the analysis procedure described above. The entry denoted with a light blue star shows signal from the backlighter plasma, focused to a different line on the detector, owing to poor shielding. Despite efforts to mask the parasitic signal, this might have resulted in an additional, systematic offset. The errors shown in Fig. 4 were estimated from the uncertainties of the ratio of elastic to inelastic scattering obtained by the Bayesian fitting routine, the sensitivity to the choice of background, and small shifts in the energy calibration, which might be caused, for example, by a misalignment of the laser with respect to the pinhole. The errors in $x_{\mathrm{el}}/x_{\mathrm{inel}}$ were mapped to temperatures by approximating the relationship between the two quantities as linear (as is suggested by the DFT-MD simulations presented in Fig. 2). The notable uncertainties are rooted in the high background and noise ratio of the signal and are planned to be reduced in follow-up studies with improved shielding.

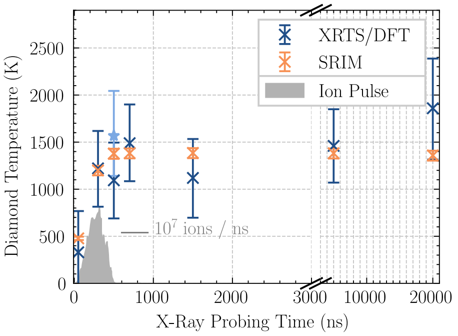

FIG. 4. Comparison of the temperatures obtained from the ratio of elastic to inelastic scattering in the XRTS spectrum (blue) with those from SRIM[29] simulations of energy deposited within the sample corrected for slight shot-to-shot variations in the ion number (orange). While both methods suggest comparable temperatures, XRTS measures a slightly colder diamond, on average. However, later delays coincide with a change in the diffraction pattern, described in Sec. IV. The orange points neglect effects of cooling and heat transfer within the diamond. This simplification was justified by thermal simulations including conductivity with the ANSYS software package for the maximal ion numbers achieved in our experiments, suggesting that these effects have minor implications on the timescales examined. The ion flux as measured by a fast current transformer for a representative event is shown by the gray area, where the axis is given by the solid horizontal line.

In Fig. 4, we compare the results of our method with temperatures estimated from the number of ions entering our target chamber. To link the latter quantity to temperatures, we calculated the energy deposition of the ions in the sample with SRIM.[29] For these simulations, the temporal shape of the ion pulse was approximated by a $\sin^2 t$ profile, fitting the signal measured by a fast current transformer in the beam's path. The presented calculations account for the inhomogeneous conditions in the target by calculating a spatial average of the temperatures, weighted by the X-ray intensity on the diamond, which was obtained via the ray tracing code. To verify the applicability of the one-dimensional SRIM calculations, we compared the result with those of full 3D simulations using the FLUKA code[41,42] for energy deposition. Both methods agree reasonably well, with deviations smaller than 10%. The latter results were additionally used as inputs for calculations applying the ANSYS 2023 R2 software package to model the effects of heat transfer and cooling of the sample. We found that both effects only lead to small corrections, even at the biggest delays investigated for temperatures below 2000 K. Therefore, we neglected these contributions when simulating individual shots. Similar calculations for an identical setup (but different sample materials) found decent agreement with benchmark pyrometry measurements.[27] While both methods indicate similar temperatures around, or even exceeding, 1300–1400 K, the temperatures obtained by the XRTS technique are on average slightly lower than those from the SRIM simulations.

IV. X-RAY DIFFRACTION

Complementary to the technique of XRTS, we fielded spatially resolved XRD. For the same reason that the ratio of elastic to inelastic scattering increases with temperature, the XRD signal is expected to decrease as the sample heats up. This behavior is captured in the Debye–Waller factor.[43] However, owing to the high Debye temperature of diamond, our DFT-MD simulations indicate that the intensity of the (111) peak would recede by less than 4% at 1500 K. Hence, for the temperatures reached, we do not expect a notable change of the diffraction signal due to diamond heating alone.

By contrast, a transition to graphite would result in a notable change of the diffraction pattern. For the ion numbers realized, the center of our sample is predicted to reach peak temperatures around 1900 K. Under these conditions, graphitization of diamond has been observed in vacuum.[18]

Diffraction patterns recorded for different delays between ion and PHELIX pulses are plotted in Fig. 5. Each recording shows three distinct continuous lines which are caused by the spectrum of the backlighter. Because of the finite size of the source on the diamond (~1 mm in diameter), the Laue spots are smeared out despite the sample being monocrystalline. As the rotation of the diamond—and hence the position of the (111) reflection—could not be perfectly reproduced between targets, the position of the pattern on the IP varies for different shots. Figure 5 accounts for that by displaying the diffraction data shifted so that the recordings align on a common ring. The presented data were scaled by the X-ray intensity on the monitor spectrometer and corrected for the decay of the signal on the IP during the time between recording and scanning. We then removed a constant background.

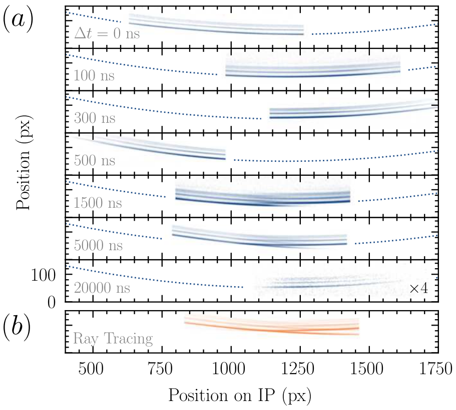

FIG. 5. (a) XRD signals recorded on IPs at different X-ray probing times Δt. Each diffraction pattern shows three rings, caused by the He$_\alpha$ main, intercombination, and lithium-like lines from the Ti backlighter. Because the source was significantly extended on the sample, the Laue spots of the monocrystalline material are smeared into circular segments. The measured two-dimensional data have been offset horizontally to align on these circles (denoted by dotted lines to guide the eye). The intensity of individual plots has been corrected for the source intensity and the decay of the IP signal. For the longest delay of $\Delta t = 20\,000$ ns, only a faint signal was detected, and the intensity has been scaled up by a factor of four for better readability. For $\Delta t = 1500$ and 5000 ns, the signal changes qualitatively: the pattern no longer shows three concentric circles, but the formerly continuous rings seem to break apart. We can obtain similar images with our ray tracing code when splitting our sample in two parts along the ion beam axis and rotating the upper half by 5°: see the orange plot in (b).

The collected data show no clear signs of graphitization. For delays up to 500 ns, the signal does not differ noticeably from that of an unheated sample. At longer delays, however, the elongated Laue spots start to break apart. We can reproduce this feature well with our ray tracing software by splitting the cylinder representing the diamond sample in half, along the ion beam direction, and rotating the upper part by few degrees.

While we are currently lacking a conclusive understanding of what is happening to the sample at longer delays, we consider the XRD signal as a hint that our sample might break after irradiation with the ion beam. The fact that the longest delay only shows a faint diffraction pattern might support this hypothesis, as parts of the sample might have moved too far to be captured in the field of view of the IP. Anyway, the change in the XRD signal demonstrates how this method can provide additional insight into the sample that is not apparent in XRTS and is required as a complementary diagnostic when moving to higher temperatures to identify the onset of graphitization.

V. CONCLUSIONS AND OUTLOOK

We have presented a method to leverage the widely used technique of X-ray Thomson scattering as a temperature diagnostic for diamond samples heated by heavy ion beams, relying on DFT-MD and ray tracing simulations. The approach is applicable even under relatively cold conditions, where optical pyrometry fails. Combining this measurement with an XRD diagnostic has allowed us to investigate the microscopic structure of the material, which does not show *in situ* evidence for graphitization of the diamond and provides hints that our sample breaks on a macroscopic level.

Using heavy ions as a driver yields some unique challenges for the detection of the XRTS signal, since the a substantial background is induced by the ion beam hitting the sample. We have accommodated this by using both physical shielding and post-processing of the data, relying on a neural network to identify faulty pixels. Furthermore, the experiment has probed a wide range of scattering vectors, owing to the large size of the X-ray source on the sample, and so our analysis required that we perform ray tracing simulations of the full setup, from the backlighter to the detector.

The temperatures inferred from the scattering signal appear to be compatible with estimates from ion stopping power simulations. For delays longer than 1 μs, we have recorded a qualitative change in the XRD signal, suggesting a major alteration in our sample. Hence, the temperature measurement for those delays might show a systematic error. While we have not identified graphitization of our sample, raising the number of ions and consequently the temperatures—as will be possible with the SIS100 accelerator—seems a promising route to study this phenomenon, since it is predicted to be vastly accelerated by a small increase in temperature.[19]

The work described here represents an important step toward a temperature diagnostic for WDM that can provide insight into the bulk of the probed material rather than just the surface properties accessible by optical methods. Such a tool is highly desirable, for example, in view of the novel experimental capabilities being opened up for WDM research by FAIR, allowing the creation of samples of millimeter size.

SUPPLEMENTARY MATERIAL

The supplementary material extends individual aspects of the analysis. We report on simulation of the backlighter spectrum and benchmark it to the measurements of the monitor spectrometer. Additionally, we demonstrate the capability of the combined LR-TDDFT and ray tracing simulations to reproduce high-resolution scattering data for cold diamond, published by Voigt *et al.*[44] We furthermore present the result of our post-processing step removing particle traces in the XRTS signal (described in Appendix C) for a representative event.

ACKNOWLEDGMENTS

The results presented here are based on experiment S489 performed at the HHT target station in the context of FAIR Phase-0 at GSI, Darmstadt (Germany). J.L. and D.K. were supported by GSI Helmholtzzentrum für Schwerionenforschung, Darmstadt as part of the R&D project SI-Grant No. URDK2224 with the University of Rostock. M.S. and R.R. acknowledge support by the Deutsche Forschungsgemeinschaft (DFG) within the Research Unit FOR 2440. The *ab initio* calculations were performed at the North-German Supercomputing Alliance (HLRN) facilities. R.B. acknowledges support by the Federal Ministry of Education and Research (BMBF) under Grant No. 05P21RFFA2. O.S.H. and D.K. were supported by the Helmholtz Association under Grant No. ERC-RA-0041.

AUTHOR DECLARATIONS

Conflict of Interest

The authors have no conflicts to disclose.

Author Contributions

J. Lütgert: Formal analysis (equal); Investigation (equal); Visualization (equal); Writing – original draft (equal); Writing – review & editing (equal). **P. Hesselbach**: Formal analysis (equal); Investigation (equal); Writing – original draft (equal); Writing – review & editing (equal). **M. Schörner**: Formal analysis (equal); Writing – original draft (equal); Writing – review & editing (equal). **V. Bagnoud**: Conceptualization (equal); Investigation (equal). **R. Belikov**: Investigation (equal). **P. Drechsel**: Formal analysis (equal). **B. Heuser**: Formal analysis (equal); Writing – review & editing (equal). **O. S. Humphries**: Investigation (equal). **P. Katrik**: Formal analysis (equal). **B. Lindqvist**: Investigation (equal). **C. Qu**: Formal analysis (equal). **R. Redmer**: Supervision (equal); Writing – review & editing (equal). **D. Riley**: Conceptualization (equal); Investigation (equal). **G. Schaumann**: Investigation (equal). **S. Schumacher**: Formal analysis (equal); Writing – review & editing (equal). **A. Tauschwitz**: Investigation (equal). **D. Varentsov**: Investigation (equal). **K. Weyrich**: Investigation (equal). **X. Yu**: Investigation (equal). **B. Zielbauer**: Investigation (equal). **Zs. Major**: Conceptualization (equal); Formal analysis (equal); Investigation (equal); Writing – original draft (equal); Writing – review & editing (equal). **P. Neumayer**: Conceptualization (equal); Formal analysis (equal); Investigation (equal); Supervision (equal); Writing – review & editing (equal). **D. Kraus**: Conceptualization (equal); Formal analysis (equal); Investigation (equal); Supervision (equal); Writing – original draft (equal); Writing – review & editing (equal).

DATA AVAILABILITY

The data that support the findings of this study are available from the corresponding authors upon reasonable request.

APPENDIX A: DFT-MD SIMULATIONS

All DFT-MD simulations for this work were performed with the Vienna *ab initio* Simulation Package (VASP).[45–47] The electronic and ionic parts were decoupled by the Born–Oppenheimer approximation, and, for fixed ion positions, the electronic problem was solved in the finite temperature DFT approach[48] using a projector augmented wave pseudopotential (labeled `PAW_PBE C_h`)[49,50] and the Perdew–Burke–Ernzerhof functional[51] for the exchange-correlation contribution. A $4 \times 4 \times 4$ Monkhorst–Pack sampling[52] was employed for k space, and a plane wave cutoff energy of 1000 eV was used. The forces and energies predicted by DFT were learned by a Behler–Parrinello high-dimensional neural network potential (HDNNP)[53] implemented in the n2p2 software package.[54–56] The symmetry functions were chosen according to the scheme presented by Imbalzano *et al.*,[57] with a maximum cutoff radius of 4 Å. The trained HDNNP was used to compute the electronic forces on the ions in the MD simulation within the LAMMPS software package.[58] For more details of this method, see Ref. 59. The temperature control in all MD simulations was performed by a Nosé–Hoover thermostat.[60,61] The inelastic contribution to XRTS was computed from the dielectric function, which we computed in the framework of linear response time-dependent DFT within the GPAW simulation code,[62–65] with an energy cutoff of 100 eV. Local field effects of the lattice were taken into account by inverting the dielectric matrix,[36,66] and electron correlations were considered in the random phase approximation. For the DFT-MD simulations, 64 atoms were used, while the MD simulations driven by the HDNNP were performed at 64, 1000, 8000, and 27 000 atoms. For the LR-TDDFT calculations, 8 atoms were considered.

APPENDIX B: RAY TRACING

The ray tracing simulations were performed with an in-house Python code, utilizing the `jax` module.[38] A set of rays was initialized on the titanium backlighter foil with positions drawn from a Gaussian distribution with 100 μm FWHM in both dimensions. The directions of the rays were distributed uniformly over a cone with an opening angle of 45°. We verified that increasing this angle does not result in a change of the distribution of rays on the diamond. The energies of the rays were sampled from the spectral distribution of the Ti He$_\alpha$ emission, obtained from PrismSPECT simulation software, fitting the recorded monitor spectra of the individual shots.

For each iteration, 10^8 rays were traced in parallel. For every component in the beam's path, the intersection of the rays and the component's surface was calculated analytically, before the properties of the rays were modified on the basis of the specific type of component.

To model the X-ray diffraction signal, we calculated the angle between the incoming rays and the normal on the (111) crystal plane and reflected only those rays for which the angle of incidence was equal to the Bragg angle

$$\theta_B = \arcsin\left(\frac{ch}{2dE}\right) \tag{B1}$$

up to a small acceptance range. Here, c denotes the speed of light, h Planck's constant, d the distance between two crystal planes [$d = (1/\sqrt{3}) \times 3.57$ Å in our setup], and E the photon energy. The rays were further propagated toward a planar detector.

To simulate the spectrometers, we implemented a Monte Carlo approach for the mosaic crystals in a similar fashion to the `mmpxrt` code of Šmíd *et al.*[39] For each incoming ray, we randomly drew an angle α from a Lorentzian distribution with a FWHM of the mosaicity of the crystal. In a second step, we analytically calculated and randomly selected one of the normed vectors $\mathbf{n}_c$ that satisfied the following two conditions:

1. The angle between $\mathbf{n}_c$ and the crystal normal is equal to α.
2. The angle between $\mathbf{n}_c$ and the incident ray is equal to $\pi/2 - \theta_B$, i.e., the ray satisfies the Bragg condition [Eq. (B1)] if reflected on a surface with normal $\mathbf{n}_c$.

If such an $\mathbf{n}_c$ was found, we set this vector as the "crystallite normal" and reflected the incoming ray on the surface thus defined. In the case that the two cones did not intersect, the ray was discarded, instead. However, this method would over-emphasize the contribution of normals with large values of α, since the crystallite normals could be oriented at any azimuthal angle defined by the first of the above conditions, not only those that also satisfy the second condition. We therefore introduced a corrective factor to the reflected ray intensity, proportional to $1/\sin\alpha$. A sketch of this geometry is provided in Fig. 6.

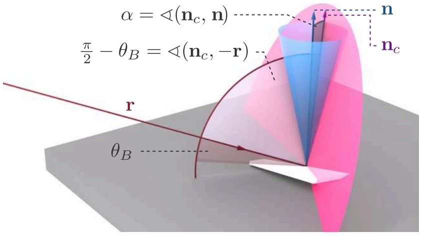

FIG. 6. Sketch visualizing the selection of crystallite normals when simulating mosaic crystals in our ray tracing code. All vectors that enclose the angle α with the surface normal **n** form the mantle of the blue cone. From this set of potential crystallite normals, we identify those vectors $\mathbf{n}_c$ that also satisfy the Bragg condition, i.e., we require that the angle between the incoming ray **r** and $\mathbf{n}_c$ be equal to $\pi/2 - \theta_B$ (the pink cone depicts all vectors for which this is the case). To account for the probability of both conditions being realized for a specific ray and given α, we reduce the weight of the reflected ray by a factor proportional to $\sin\alpha$.

To avoid divergence, we defined an angle in which all rays are reflected. For this angle, we chose the FWHM of the intrinsic crystal rocking curve, which amounts to 0.006° for HOPG.[39] In a final step, we uniformly randomized the direction of the light rays in the cone given by this angle. This, again, is in accordance with the procedure of Šmíd *et al.*[39]

For the calculation of the monitor spectrum, we assumed the rays to be unchanged by the diamond sample.

When simulating the XRTS signal, the directions of the rays were uniformly distributed in a wide cone facing the detector after hitting the diamond sample. If inelastic scattering was simulated, the shift in photon energy was drawn for each ray, individually, according to the results of the LR-TDDFT calculation.

APPENDIX C: MASKING OF PROMINENT PARTICLE TRACES

Our diagnostics clearly showed faulty signal—even on shots where the target was irradiated only with ions, but not X rays. Notably, we identified several traces of connected pixels with high intensity (see Fig. S3 in the supplementary material). These might be caused by charged particles, according to simulations of the interaction of the ions with entrance window and target, performed with FLUKA.[41,42] We trained a U-net convolutional neural network, often used for the task of image segmentation,[67] to mask these pixels. The network was implemented using the Python package `PyTorch`[68] and trained on 5000 artificially created black-and-white images.

To apply the model to our data, we had to threshold the recording first and divide it into 64 × 64 px^2 blocks. We repeated the latter step with an offset of half the block size and applied the model to all the resulting subimages, classifying only those pixels as parasitic that were masked in both runs. This additional step was taken to avoid an over-masking of pixels at the edges of the subimages.

An example of such a mask and the resulting cleaned image are depicted in Fig. S3 of the supplementary material. For our further analysis, we discarded all pixels masked by the network.

REFERENCES

[1] S. H. Glenzer and R. Redmer, "X-ray Thomson scattering in high energy density plasmas," Rev. Mod. Phys. **81**, 1625–1663 (2009).

[2] A. Descamps, B. K. Ofori-Okai, K. Appel, V. Cerantola, A. Comley, J. H. Eggert, L. B. Fletcher, D. O. Gericke, S. Göde, O. Humphries, O. Karnbach, A. Lazicki, R. Loetzsch, D. McGonegle, C. A. J. Palmer, C. Plueckthun, T. R. Preston, R. Redmer, D. G. Senesky, C. Strohm, I. Uschmann, T. G. White, L. Wollenweber, G. Monaco, J. S. Wark, J. B. Hastings, U. Zastrau, G. Gregori, S. H. Glenzer, and E. E. McBride, "An approach for the measurement of the bulk temperature of single crystal diamond using an X-ray free electron laser," Sci. Rep. **10**, 14564 (2020).

[3] .T. Döppner, M. Bethkenhagen, D. Kraus, P. Neumayer, D. A. Chapman, B. Bachmann, R. A. Baggott, M. P. Böhme, L. Divol, R. W. Falcone, L. B. Fletcher, O. L. Landen, M. J. MacDonald, A. M. Saunders, M. Schörner, P. A. Sterne, J. Vorberger, B. B. L. Witte, A. Yi, R. Redmer, S. H. Glenzer, and D. O. Gericke, "Observing the onset of pressure-driven K-shell delocalization," Nature **618**, 270–275 (2023).

[4] D. Ranjan, K. Ramakrishna, K. Voigt, O. S. Humphries, B. Heuser, M. G. Stevenson, J. Lütgert, Z. He, C. Qu, S. Schumacher, P. T. May, A. Amouretti, K. Appel, E. Brambrink, V. Cerantola, D. Chekrygina, L. B. Fletcher, S. Göde, M. Harmand, N. J. Hartley, S. P. Hau-Riege, M. Makita, A. Pelka, A. K. Schuster, M. Šmíd, T. Toncian, M. Zhang, T. R. Preston, U. Zastrau, J. Vorberger, and D. Kraus, "Toward using collective x-ray Thomson scattering to study C–H demixing and hydrogen metallization in warm dense matter conditions," Phys. Plasmas **30**, 052702 (2023).

[5] A.-C. Dippel, H.-P. Liermann, J. T. Delitz, P. Walter, H. Schulte-Schrepping, O. H. Seeck, and H. Franz, "Beamline P02.1 at PETRA III for high-resolution and high-energy powder diffraction," J. Synchrotron Radiat. **22**, 675–687 (2015).

[6] M. G. Stevenson, E. J. Pace, C. V. Storm, S. E. Finnegan, G. Garbarino, C. W. Wilson, D. McGonegle, S. G. Macleod, and M. I. McMahon, "Pressure-induced bcc-rhombohedral phase transition in vanadium metal," Phys. Rev. B **103**, 134103 (2021).

[7] D. Kraus, J. Vorberger, N. J. Hartley, J. Lütgert, M. Rödel, D. Chekrygina, T. Döppner, T. van Driel, R. W. Falcone, L. B. Fletcher, S. Frydrych, E. Galtier, D. O. Gericke, S. H. Glenzer, E. Granados, Y. Inubushi, N. Kamimura, K. Katagiri, M. J. MacDonald, A. J. MacKinnon, T. Matsuoka, K. Miyanishi, E. E. McBride, I. Nam, P. Neumayer, N. Ozaki, A. Pak, A. Ravasio, A. M. Saunders, A. K. Schuster, M. G. Stevenson, K. Sueda, P. Sun, T. Togashi, K. Voigt, M. Yabashi, and T. Yabuuchi, "Indirect evidence for elemental hydrogen in laser-compressed hydrocarbons," Phys. Rev. Res. **5**, L022023 (2023).

[8] H. Hirai, K. Konagai, T. Kawamura, Y. Yamamoto, and T. Yagi, "Polymerization and diamond formation from melting methane and their implications in ice layer of giant planets," Phys. Earth Planet. Inter. **174**, 242–246 (2009).

[9] R. Chau, S. Hamel, and W. J. Nellis, "Chemical processes in the deep interior of Uranus," Nat. Commun. **2**, 203 (2011).

[10] D. Kraus, J. Vorberger, A. Pak, N. J. Hartley, L. B. Fletcher, S. Frydrych, E. Galtier, E. J. Gamboa, D. O. Gericke, S. H. Glenzer, E. Granados, M. J. MacDonald, A. J. MacKinnon, E. E. McBride, I. Nam, P. Neumayer, M. Roth, A. M. Saunders, A. K. Schuster, P. Sun, T. van Driel, T. Döppner, and R. W. Falcone, "Formation of diamonds in laser-compressed hydrocarbons at planetary interior conditions," Nat. Astron. **1**, 606–611 (2017).

[11] Z. He, M. Rödel, J. Lütgert, A. Bergermann, M. Bethkenhagen, D. Chekrygina, T. E. Cowan, A. Descamps, M. French, E. Galtier, A. E. Gleason, G. D. Glenn, S. H. Glenzer, Y. Inubushi, N. J. Hartley, J.-A. Hernandez, B. Heuser, O. S. Humphries, N. Kamimura, K. Katagiri, D. Khaghani, H. J. Lee, E. E. McBride, K. Miyanishi, B. Nagler, B. Ofori-Okai, N. Ozaki, S. Pandolfi, C. Qu, D. Ranjan, R. Redmer, C. Schoenwaelder, A. K. Schuster, M. G. Stevenson, K. Sueda, T. Togashi, T. Vinci, K. Voigt, J. Vorberger, M. Yabashi, T. Yabuuchi, L. M. V. Zinta, A. Ravasio, and D. Kraus, "Diamond formation kinetics in shock-compressed C–H–O samples recorded by small-angle x-ray scattering and x-ray diffraction," Sci. Adv. **8**, eabo0617 (2022).

[12] N. A. Tahir, V. Bagnoud, P. Neumayer, A. R. Piriz, and S. A. Piriz, "Production of diamond using intense heavy ion beams at the FAIR facility and application to planetary physics," Sci. Rep. **13**, 1459 (2023).

[13] T. J. Volz, S. J. Turneaure, S. M. Sharma, and Y. M. Gupta, "Role of graphite crystal structure on the shock-induced formation of cubic and hexagonal diamond," Phys. Rev. B **101**, 224109 (2020).

[14] M. D. Knudson, M. P. Desjarlais, A. Becker, R. W. Lemke, K. R. Cochrane, M. E. Savage, D. E. Bliss, T. R. Mattsson, and R. Redmer, "Direct observation of an abrupt insulator-to-metal transition in dense liquid deuterium," Science **348**, 1455–1460 (2015).

[15] D. Kraus, J. Vorberger, D. O. Gericke, V. Bagnoud, A. Blažević, W. Cayzac, A. Frank, G. Gregori, A. Ortner, A. Otten, F. Roth, G. Schaumann, D. Schumacher, K. Siegenthaler, F. Wagner, K. Wünsch, and M. Roth, "Probing the complex ion structure in liquid carbon at 100 GPa," Phys. Rev. Lett. **111**, 255501 (2013).

[16] D. Kraus, A. Ravasio, M. Gauthier, D. O. Gericke, J. Vorberger, S. Frydrych, J. Helfrich, L. B. Fletcher, G. Schaumann, B. Nagler, B. Barbrel, B. Bachmann, E. J. Gamboa, S. Göde, E. Granados, G. Gregori, H. J. Lee, P. Neumayer, W. Schumaker, T. Döppner, R. W. Falcone, S. H. Glenzer, and M. Roth, "Nanosecond formation of diamond and lonsdaleite by shock compression of graphite," Nat. Commun. **7**, 10970 (2016).

[17] K. Schoenberg, V. Bagnoud, A. Blazevic, V. E. Fortov, D. O. Gericke, A. Golubev, D. H. H. Hoffmann, D. Kraus, I. V. Lomonosov, V. Mintsev, S. Neff, P. Neumayer, A. R. Piriz, R. Redmer, O. Rosmej, M. Roth, T. Schenkel, B. Sharkov, N. A. Tahir, D. Varentsov, and Y. Zhao, "High-energy-density-science capabilities at the facility for Antiproton and ion research," Phys. Plasmas **27**, 043103 (2020).

[18] T. Evans and P. F. James, "A study of the transformation of diamond to graphite," Proc. R. Soc. London, Ser. A **277**, 260–269 (1964).

[19] G. Davies and T. Evans, "Graphitization of diamond at zero pressure and at a high pressure," Proc. R. Soc. London, Ser. A **328**, 413–427 (1972).

[20] P. Heimann, N. J. Hartley, I. Inoue, V. Tkachenko, A. Antoine, F. Dorchies, R. Falcone, J. Gaudin, H. Höppner, Y. Inubushi, K. J. Kapcia, H. J. Lee, V. Lipp, P. Martinez, N. Medvedev, F. Tavella, S. Toleikis, M. Yabashi, T. Yabuuchi, J. Yamada, and B. Ziaja, "Non-thermal structural transformation of diamond driven by x-rays," Struct. Dyn. **10**, 054502 (2023).

[21] V. Lipp, V. Tkachenko, M. Stransky, B. Aradi, T. Frauenheim, and B. Ziaja, "Density functional tight binding approach utilized to study x-ray-induced transitions in solid materials," Sci. Rep. **12**, 1551 (2022).

[22] J. Gaudin, N. Medvedev, J. Chalupský, T. Burian, S. Dastjani-Farahani, V. Hájková, M. Harmand, H. O. Jeschke, L. Juha, M. Jurek, D. Klinger, J. Krzywinski, R. A. Loch, S. Moeller, M. Nagasono, C. Ozkan, K. Saksl, H. Sinn, R. Sobierajski, P. Sovák, S. Toleikis, K. Tiedtke, M. Toufarová, T. Tschentscher, V. Vorlíček, L. Vyšín, H. Wabnitz, and B. Ziaja, "Photon energy dependence of graphitization threshold for diamond irradiated with an intense XUV FEL pulse," Phys. Rev. B **88**, 060101 (2013).

[23] F. Tavella, H. Höppner, V. Tkachenko, N. Medvedev, F. Capotondi, T. Golz, Y. Kai, M. Manfredda, E. Pedersoli, M. J. Prandolini, N. Stojanovic, T. Tanikawa, U. Teubner, S. Toleikis, and B. Ziaja, "Soft x-ray induced femtosecond solid-to-solid phase transition," High Energy Density Phys. **24**, 22–27 (2017).

[24] W. Trischuk, M. Artuso, F. Bachmair, L. Bäni, M. Bartosik, V. Bellini, V. Belyaev, B. Bentele, E. Berdermann, P. Bergonzo, A. Bes, J.-M. Brom, M. Bruzzi, M. Cerv, C. Chau, G. Chiodini, D. Chren, V. Cindro, G. Claus, J. Collot, S. Costa, J. Cumalat, A. Dabrowski, R. D'Alessandro, W. de Boer, B. Dehning, D. Dobos, W. Dulinski, V. Eremin, R. Eusebi, G. Forcolin, J. Forneris, H. Frais-Kölbl, K. Gan, M. Gastal, M. Goffe, J. Goldstein, A. Golubev, L. Gonella, A. Gorišek, L. Graber, E. Grigoriev, J. Grosse-Knetter, M. Guthoff, I. Haughton, D. Hidas, D. Hits, M. Hoeferkamp, T. Hofmann, J. Hosslet, J.-Y. Hostachy, F. Hügging, H. Jansen, J. Janssen, H. Kagan, K. Kanxheri, G. Kasieczka, R. Kass, F. Kassel, M. Kis, G. Kramberger, S. Kuleshov, A. Lacoste, S. Lagomarsino, A. Lo Giudice, C. Maazouzi, I. Mandic, C. Manfredotti, C. Mathieu, N. McFadden, G. McGoldrick, M. Menichelli, M. Mikuž, A. Morozzi, J. Moss, R. Mountain, S. Murphy, A. Oh, P. Olivero, G. Parrini, D. Passeri, M. Pauluzzi, H. Pernegger, R. Perrino, F. Picollo, M. Pomorski, R. Potenza, A. Quadt, A. Re, G. Riley, S. Roe, M. Sapinski, M. Scaringella, S. Schnetzer, T. Schreiner, S. Sciortino, A. Scorzoni, S. Seidel, L. Servoli, A. Sfyrla, G. Shimchuk, S. Smith, B. Sopko, V. Sopko, S. Spagnolo, S. Spanier, K. Stenson, R. Stone, C. Sutera, A. Taylor, M. Traeger, D. Tromson, W. Trischuk, C. Tuve, L. Uplegger, J. Velthuis, N. Venturi, E. Vittone, S. Wagner, R. Wallny, J. Wang, P.

Weilhammer, J. Weingarten, C. Weiss, T. Wengler, N. Wermes, M. Yamouni, and M. Zavrtanik, "Diamond particle detectors for high energy physics," Nucl. Part. Phys. Proc. **273–275**, 1023–1028 (2016).

[25] A. K. Schuster, K. Voigt, B. Klemmed, N. J. Hartley, J. Lütgert, M. Zhang, C. Bähtz, A. Benad, C. Brabetz, T. Cowan, T. Döppner, D. J. Erb, A. Eychmüller, S. Facsko, R. W. Falcone, L. B. Fletcher, S. Frydrych, G. C. Ganzenmüller, D. O. Gericke, S. H. Glenzer, J. Grenzer, U. Helbig, S. Hiermaier, R. Hübner, A. Laso Garcia, H. J. Lee, M. J. MacDonald, E. E. McBride, P. Neumayer, A. Pak, A. Pelka, I. Prencipe, A. Prosvetov, A. Rack, A. Ravasio, R. Redmer, D. Reemts, M. Rödel, M. Schoelmerich, D. Schumacher, M. Tomut, S. J. Turner, A. M. Saunders, P. Sun, J. Vorberger, A. Zettl, and D. Kraus, "Recovery of release cloud from laser shock-loaded graphite and hydrocarbon targets: In search of diamonds," J. Phys. D: Appl. Phys. **56**, 025301 (2022).

[26] T. Stöhlker, V. Bagnoud, K. Blaum, A. Blazevic, A. Bräuning-Demian, M. Durante, F. Herfurth, M. Lestinsky, Y. Litvinov, S. Neff, R. Pleskac, R. Schuch, S. Schippers, D. Severin, A. Tauschwitz, C. Trautmann, D. Varentsov, and E. Widmann, "APPA at FAIR: From fundamental to applied research," Nucl. Instrum. Methods Phys. Res., Sect. B **365**, 680–685 (2015).

[27] P. Hesselbach, J. Lütgert, V. Bagnoud, R. Belikov, O. Humphries, B. Lindqvist, G. Schaumann, A. Tauschwitz, D. Varentsov, K. Weyrich, B. Winkler, X. Yu, B. Zielbauer, D. Kraus, D. Riley, Zs. Major, and P. Neumayer, "Platform for combined heavy-ion/high-energy laser experiments," (unpublished) (2024).

[28] Zs. Major, U. Eisenbarth, B. Zielbauer, C. Brabetz, J. B. Ohland, Y. Zobus, S. Roeder, D. Reemts, S. Kunzer, S. Götte, D. Neidherr, J. Hornung, P. Kewes, D. Schumacher, D. Beck, P. Hesselbach, M. Malki, P. Neumayer, K. Weyrich, A. Tauschwitz, and V. Bagnoud, "High-energy laser facility PHELIX at GSI: Latest advances and extended capabilities," High Power Laser Sci. Eng (published online) (2024).

[29] J. F. Ziegler, M. Ziegler, and J. Biersack, "SRIM—The stopping and range of ions in matter (2010)," Nucl. Instrum. Methods Phys. Res., Sect. B **268**, 1818–1823 (2010).

[30] L. v Hámos, "Röntgenspektroskopie und Abbildung mittels gekrümmter Kristallreflektoren. I. Geometrisch-optische Betrachtungen," Ann. Phys. **409**, 716–724 (1933).

[31] J. Chihara, "Interaction of photons with plasmas and liquid metals-photoabsorption and scattering," J. Phys.: Condens. Matter **12**, 231–247 (2000).

[32] G. Gregori, S. H. Glenzer, F. J. Rogers, S. M. Pollaine, O. L. Landen, C. Blancard, G. Faussurier, P. Renaudin, S. Kuhlbrodt, and R. Redmer, "Electronic structure measurements of dense plasmas," Phys. Plasmas **11**, 2754–2762 (2004).

[33] R. W. James, "The Optical Principles of the Diffraction Of X-Rays," in *The Crystalline State*, repr ed (George Bell & Sons, Ltd., London, 1962), Vol. 2.

[34] A. Pelka, G. Gregori, D. O. Gericke, J. Vorberger, S. H. Glenzer, M. M. Günther, K. Harres, R. Heathcote, A. L. Kritcher, N. L. Kugland, B. Li, M. Makita, J. Mithen, D. Neely, C. Niemann, A. Otten, D. Riley, G. Schaumann, M. Schollmeier, A. Tauschwitz, and M. Roth, "Ultrafast melting of carbon induced by intense proton beams," Phys. Rev. Lett. **105**, 265701 (2010).

[35] L. Pauling and J. Sherman, "Screening constants for many-electron atoms," *The Calculation and Interpretation of X-Ray Term Values, and the Calculation of Atomic Scattering Factors* (Akademische Verlagsgesllschaft M.B.H, Leipzig, 1932).

[36] M. Schörner, M. Bethkenhagen, T. Döppner, D. Kraus, L. B. Fletcher, S. H. Glenzer, and R. Redmer, "X-ray Thomson scattering spectra from density functional theory molecular dynamics simulations based on a modified Chihara formula," Phys. Rev. E **107**, 065207 (2023).

[37] J. MacFarlane, I. Golovkin, P. Woodruff, D. Welch, B. Oliver, T. Mehlhorn, and R. Campbell, "Simulation of the ionization dynamics of aluminum irradiated by intense short-pulse lasers," Proc. Inertial Fusion Sciences and Applications 2003 p. 457 (2004).

[38] J. Bradbury, R. Frostig, P. Hawkins, M. J. Johnson, C. Leary, D. Maclaurin, G. Necula, A. Paszke, J. VanderPlas, S. Wanderman-Milne, and Q. Zhang, *JAX: Composable transformations of Python + NumPy programs*, 2018.

[39] M. Šmíd, X. Pan, and K. Falk, "X-ray spectrometer simulation code with a detailed support of mosaic crystals," Comput. Phys. Commun. **262**, 107811 (2021).

[40] J. Salvatier, T. V. Wiecki, and C. Fonnesbeck, "Probabilistic programming in Python using PyMC$_3$," Peer J. Comput. Sci. **2**, e55 (2016).

[41] A. Ferrari, P. Sala, A. Fasso, and J. Ranft, *FLUKA: A Multi-Particle Transport Code* (CERN, Geneva, 2005)

[42] T. Böhlen, F. Cerutti, M. Chin, A. Fassò, A. Ferrari, P. Ortega, A. Mairani, P. Sala, G. Smirnov, and V. Vlachoudis, "The FLUKA code: Developments and challenges for high energy and medical applications," Nucl. Data Sheets **120**, 211–214 (2014).

[43] W. J. Murphy, A. Higginbotham, J. S. Wark, and N. Park, "Molecular dynamics simulations of the Debye–Waller effect in shocked copper," Phys. Rev. B **78**, 014109 (2008).

[44] K. Voigt, M. Zhang, K. Ramakrishna, A. Amouretti, K. Appel, E. Brambrink, V. Cerantola, D. Chekrygina, T. Döppner, R. W. Falcone, K. Falk, L. B. Fletcher, D. O. Gericke, S. Göde, M. Harmand, N. J. Hartley, S. P. Hau-Riege, L. G. Huang, O. S. Humphries, M. Lokamani, M. Makita, A. Pelka, C. Prescher, A. K. Schuster, M. Šmíd, T. Toncian, J. Vorberger, U. Zastrau, T. R. Preston, and D. Kraus, "Demonstration of an x-ray Raman spectroscopy setup to study warm dense carbon at the high energy density instrument of European XFEL," Phys. Plasmas **28**, 082701 (2021).

[45] G. Kresse and J. Hafner, "*Ab initio* molecular dynamics for liquid metals," Phys. Rev. B **47**, 558–561 (1993).

[46] G. Kresse and J. Hafner, "*Ab initio* molecular-dynamics simulation of the liquid-metal–amorphous-semiconductor transition in germanium," Phys. Rev. B **49**, 14251–14269 (1994).

[47] G. Kresse and J. Furthmüller, "Efficient iterative schemes for *ab initio* total-energy calculations using a plane-wave basis set," Phys. Rev. B **54**, 11169–11186 (1996).

[48] N. D. Mermin, "Thermal properties of the inhomogeneous electron gas," Phys. Rev **137**, A1441–A1443 (1965).

[49] P. E. Blöchl, "Projector augmented-wave method," Phys. Rev. B **50**, 17953–17979 (1994).

[50] G. Kresse and D. Joubert, "From ultrasoft pseudopotentials to the projector augmented-wave method," Phys. Rev. B **59**, 1758–1775 (1999).

[51] J. P. Perdew, K. Burke, and M. Ernzerhof, "Generalized gradient approximation made simple," Phys. Rev. Lett. **77**, 3865–3868 (1996).

[52] H. J. Monkhorst and J. D. Pack, "Special points for Brillouin-zone integrations," Phys. Rev. B **13**, 5188–5192 (1976).

[53] J. Behler and M. Parrinello, "Generalized neural-network representation of high-dimensional potential-energy surfaces," Phys. Rev. Lett. **98**, 146401 (2007).

[54] T. Morawietz, A. Singraber, C. Dellago, and J. Behler, "How van der Waals interactions determine the unique properties of water," Proc. Natl. Acad. Sci. U. S. A. **113**, 8368–8373 (2016).

[55] A. Singraber, T. Morawietz, J. Behler, and C. Dellago, "Parallel multistream training of high-dimensional neural network potentials," J. Chem. Theory Comput. **15**, 3075–3092 (2019).

[56] A. Singraber, *n2p2—A neural network potential package*, 2021, computer software.

[57] G. Imbalzano, A. Anelli, D. Giofré, S. Klees, J. Behler, and M. Ceriotti, "Automatic selection of atomic fingerprints and reference configurations for machine-learning potentials," J. Chem. Phys. **148**, 241730 (2018).

[58] A. P. Thompson, H. M. Aktulga, R. Berger, D. S. Bolintineanu, W. M. Brown, P. S. Crozier, P. J. in 't Veld, A. Kohlmeyer, S. G. Moore, T. D. Nguyen, R. Shan, M. J. Stevens, J. Tranchida, C. Trott, and S. J. Plimpton, "LAMMPS—A flexible simulation tool for particle-based materials modeling at the atomic, meso, and continuum scales," Comput. Phys. Commun. **271**, 108171 (2022).

[59] M. Schörner, H. R. Rüter, M. French, and R. Redmer, "Extending ab initio simulations for the ion-ion structure factor of warm dense aluminum to the hydrodynamic limit using neural network potentials," Phys. Rev. B **105**, 174310 (2022).

[60] S. Nosé, "A unified formulation of the constant temperature molecular dynamics methods," J. Chem. Phys. **81**, 511–519 (1984).

[61] W. G. Hoover, "Canonical dynamics: Equilibrium phase-space distributions," Phys. Rev. A **31**, 1695–1697 (1985).

[62] J. J. Mortensen, L. B. Hansen, and K. W. Jacobsen, "Real-space grid implementation of the projector augmented wave method," Phys. Rev. B **71**, 035109 (2005).

[63] J. Enkovaara, C. Rostgaard, J. J. Mortensen, J. Chen, M. Dułak, L. Ferrighi, J. Gavnholt, C. Glinsvad, V. Haikola, H. A. Hansen, H. H. Kristoffersen, M. Kuisma, A. H. Larsen, L. Lehtovaara, M. Ljungberg, O. Lopez-Acevedo, P. G. Moses, J. Ojanen, T. Olsen, V. Petzold, N. A. Romero, J. Stausholm-Møller, M. Strange, G. A. Tritsaris, M. Vanin, M. Walter, B. Hammer, H. Häkkinen, G. K. H. Madsen, R. M. Nieminen, J. K. Nørskov, M. Puska, T. T. Rantala, J. Schiøtz, K. S. Thygesen, and K. W. Jacobsen, "Electronic structure calculations with GPAW: A real-space implementation of the projector augmented-wave method," J. Phys.: Condens. Matter **22**, 253202 (2010).

[64] A. Hjorth Larsen, J. Jørgen Mortensen, J. Blomqvist, I. E. Castelli, R. Christensen, M. Dułak, J. Friis, M. N. Groves, B. Hammer, C. Hargus, E. D. Hermes, P. C. Jennings, P. Bjerre Jensen, J. Kermode, J. R. Kitchin, E. Leonhard Kolsbjerg, J. Kubal, K. Kaasbjerg, S. Lysgaard, J. Bergmann Maronsson, T. Maxson, T. Olsen, L. Pastewka, A. Peterson, C. Rostgaard, J. Schiøtz, O. Schütt, M. Strange, K. S. Thygesen, T. Vegge, L. Vilhelmsen, M. Walter, Z. Zeng, and K. W. Jacobsen, "The atomic simulation environment—A Python library for working with atoms," J. Phys.: Condens. Matter **29**, 273002 (2017).

[65] J. Yan, J. J. Mortensen, K. W. Jacobsen, and K. S. Thygesen, "Linear density response function in the projector augmented wave method: Applications to solids, surfaces, and interfaces," Phys. Rev. B **83**, 245122 (2011).

[66] S. Waidmann, M. Knupfer, B. Arnold, J. Fink, A. Fleszar, and W. Hanke, "Local-field effects and anisotropic plasmon dispersion in diamond," Phys. Rev. B **61**, 10149–10153 (2000).

[67] O. Ronneberger, P. Fischer, and T. Brox, "U-net: Convolutional networks for biomedical image segmentation," in *Medical Image Computing and Computer-Assisted Intervention–MICCAI 2015* (Springer International Publishing, Cham, 2015), pp. 234–241.

[68] A. Paszke, S. Gross, F. Massa, A. Lerer, J. Bradbury, G. Chanan, T. Killeen, Z. Lin, N. Gimelshein, L. Antiga, A. Desmaison, A. Kopf, E. Yang, Z. DeVito, M. Raison, A. Tejani, S. Chilamkurthy, B. Steiner, L. Fang, J. Bai, and S. Chintala, "PyTorch: An imperative style, high-performance deep learning library," in *Advances in Neural Information Processing Systems*, edited by H. Wallach, H. Larochelle, A. Beygelzimer, F. d'Alché Buc, E. Fox and R. Garnett (Curran Associates, Inc., 2019), Vol. 32, pp. 8024–8035.